ADVANCED MATERIALS
www.advmat.de

Body-Coupled-Driven Object-Oriented Natural Interactive Interface

Jianlong Hong, Yukun Xiao, Yuqi Chen, Shengshun Duan, Shengxin Xiang, Xiao Wei, Huiyun Zhang, Lei Liu, Jun Xia, Wei Lei, Qiongfeng Shi, Chengkuo Lee,* and Jun Wu**

The metaverse progressively demands heightened sophistication in human-multi-machine collaboration, accelerating development of hybrid immersive 2D tactile and 3D spatial perception interfaces. However, current interfaces struggle with the precision and adaptability in complex human-multi-machine interaction scenarios. This paper presents a transparent stretchable sensing interface synergizing 2D tactile and 3D spatial perception through body-coupled electromagnetic coupling. Its bi-modal coupling (resistive coupling and capacitive coupling) mechanism enables micrometer-scale 2D tactile sensing alongside broad 3D spatial perception (200 mm range). The contact mode achieves calligraphy-grade trajectory reconstruction (200 µm precision) with force tactile sensing, while the non-contact mode recognizes 38 gestures at 97.11% accuracy. The interface's mechanical transparency and elasticity permit seamless integration on curved surfaces (e.g., gloves and clothes) without perceptual interference. An object-oriented human-machine interaction (HMI) framework is developed to enable single-interface control of multiple devices through electromagnetic signature recognition, enhancing collaborative efficiency. This work can inspire designs of smart interfaces in intelligent healthcare monitoring, industrial robotics coordination, and cross-domain augmented reality applications.

1. Introduction

The rapid evolution of metaverse and artificial intelligence (AI) has sparked a wave of technological innovation in human-machine interfaces,[1] particularly in lightweight, multifunctional, and wearable systems. This transformation not only reshapes how users connect with digital environments[2] but also creates an urgent demand for naturalized and intuitive interaction paradigms. Current HMI systems face dual-dimensional upgrades: At the functional architecture level, the traditional one-to-one correspondence between the control end and the controlled object linear control model struggles to meet parallel operation requirements in dynamic multitask scenarios; At the perceptual dimension level, the transition from 2D planar interaction[3] to 3D spatial interaction[4] necessitates hybrid interaction models integrating spatial awareness with precise tactile control.[5] This dual transformation positions electronic skin (e-skin) technology at the core of the next-generation metaverse interaction revolution.

As a groundbreaking technology mimicking biological skin perception mechanisms,[6] e-skin achieves precise capture of physical signals including pressure,[7,8] temperature,[9] slide,[10] and texture[11] through multimodal sensing networks (incorporating piezoresistive,[12] capacitive,[13] piezoelectric[14] and triboelectric mechanisms[15]), demonstrating unique advantages in medical monitoring,[16,17] robotic tactile sensing,[18,19] and environmental perception.[20,21] Its core value lies in establishing an intuitive interaction system aligned with human physiology.[22] By simulating natural skin perception mechanisms, it significantly reduces the cognitive load in human-computer interaction, forming the critical technical foundation for realizing "digital twin" experiences in the metaverse. However, current e-skin technologies show notable limitations in 3D spatial perception: most devices only achieve 1D proximity sensing,[23,24] failing to interpret complex gestures and spatial relationships, thereby constraining interaction freedom.[25]

Research communities have made multidimensional breakthroughs to address these technical bottlenecks. Zhou et al. proposed a 3 × 3 touchless sensor array based on triboelectricity and electrostatic induction. From the output of the nine sensors, the author used a multilayer perceptron (MLP) neural network to recognize 16 different gestures and finally achieved an average accuracy of 96.5%.[26] Similarly, Du et al. designed a 20 × 20 triboelectric proximity sensor array, which is large

J. Hong, Y. Xiao, Y. Chen, S. Duan, S. Xiang, X. Wei, H. Zhang, L. Liu, J. Xia, W. Lei, Q. Shi, J. Wu
Interdisciplinary Research Center
School of Electronic Science and Engineering
Southeast University
Nanjing 211189, China
E-mail: qiongfeng@seu.edu.cn; wujunseu@seu.edu.cn
C. Lee
Department of Electrical and Computer Engineering
National University of Singapore
Singapore 117576, Singapore
E-mail: elelc@nus.edu.sg
C. Lee
Center for Intelligent Sensors and MEMS (CISM)
National University of Singapore
Singapore 117608, Singapore

The ORCID identification number(s) for the author(s) of this article can be found under https://doi.org/10.1002/adma.202507067

DOI: 10.1002/adma.202507067

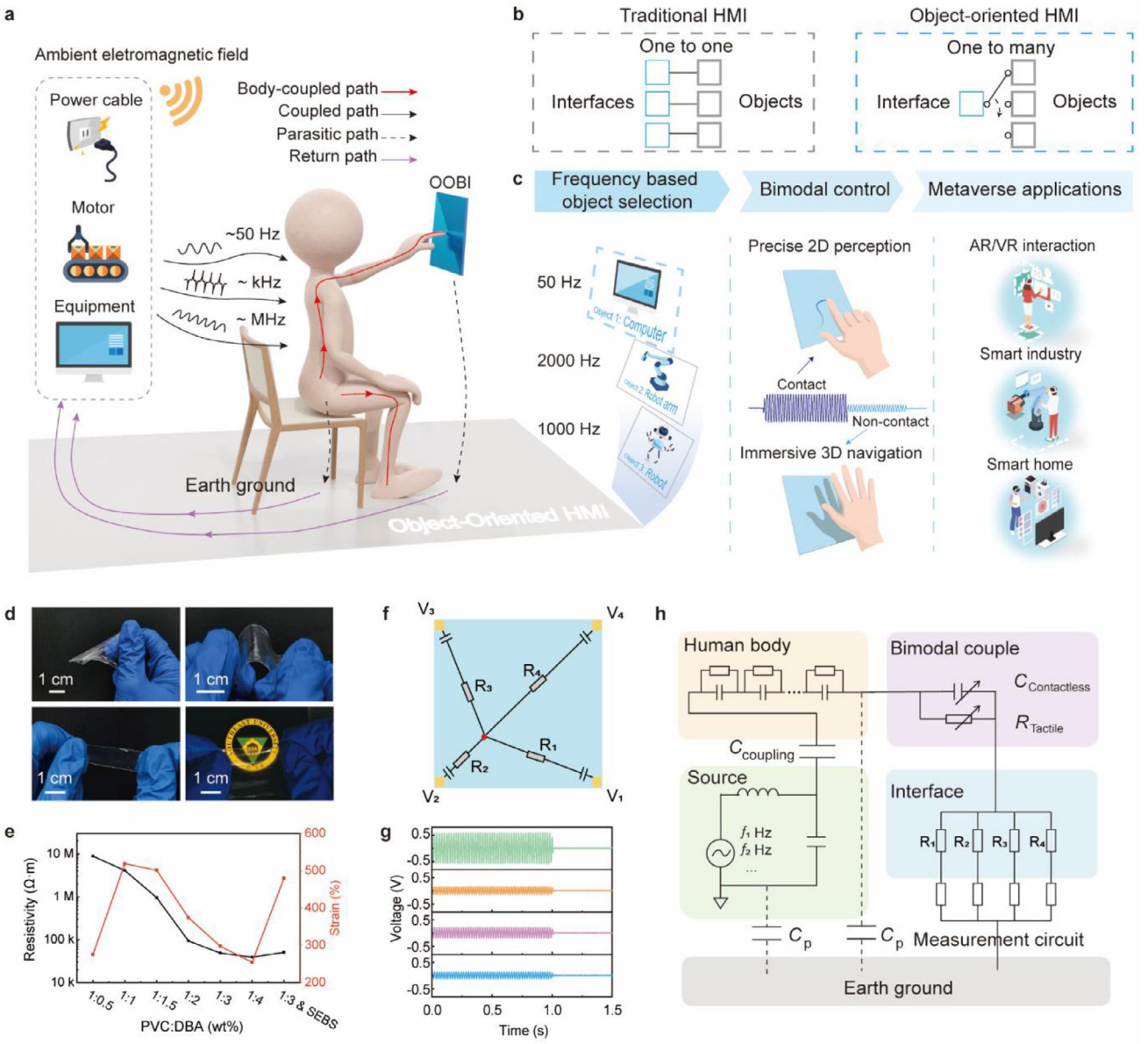

Figure 1. Ambient EM energy powered object-oriented natural human-machine interaction. a) Schematic of the OOBI powered by various ambient EM fields, such as power cable (50 Hz), motors (~MHz), and other equipment (~kHz). b) Comparison between traditional HMI and object-oriented HMI. c) Characteristics of object-oriented HMI, including object selection, bimodal control, and its potential applications. d) Optical images of the soft, thin, transparent, and stretchable interface. e) Resistivity and maximum elongation of the interface with different ratios of materials composition. f) Equivalent circuit model of interface, which has four electrodes at the corners. g) Voltage outputs of the four electrodes when the interface is touched. h) Equivalent circuit model of body coupled EM signals transmission in a close loop.

and dense enough to map the detailed 2D shape of various 3D objects.[27] However, exponential increases in sensor quantity raise cost concerns. To solve the problem, Zhou et al. recently proposed a mormyroidea-inspired capacitive coupling e-skin that could achieve 3D spatial positioning with only 5 electrodes.[25] Notably, existing solutions have yet to balance tactile resolution with spatial perception, particularly in precision scenarios like surgical robotics[28] and industrial machinery control,[29] where insufficient tactile feedback accuracy directly impacts system practicality.

In this paper, we developed a transparent and stretchable object-oriented body-coupled interface (OOBI) that integrates micrometer-scale 2D tactile precision with 3D spatial perception, addressing the critical gap between precision manipulation and immersive interaction in metaverse applications (**Figure 1a**). The OOBI achieves sub-millimeter tactile fidelity (200 μm spatial resolution) with dual-response for force and trajectory, enabling calligraphy-grade handwriting reconstruction. Additionally, its non-contact sensing modality extends interaction into 3D through a 200 mm operational range, enabling precise 3D

trajectory localization with an impressive 97.11% accuracy in recognizing 38 non-contact gestures encompassing all 26 alphabet letters. The transparent and stretchable nature of this sensing interface further enhances its versatility and adaptability, allowing it to conform to various surfaces and environments while maintaining high sensitivity and accuracy.

To resolve the complexity of multi-object interaction, we developed an object-oriented human machine interaction (HMI) framework that controls multiple objects using a single interface, enabling efficient human-multi-machine collaboration and transforming the landscape of HMI (Figure 1b). By detecting unique electromagnetic (EM) signatures from proximate devices (Figure 1c), the system intuitively selects interaction objects when they are in close proximity, mimicking the natural tendency for face-to-face communication in human interactions. Meanwhile, the architecture supports bimodal operation. According to the amplitude of voltage signals, users seamlessly transition (response time < 1 ms) between calligraphy-grade 2D perception and immersive 3D navigation without interface switching. This breakthrough bridges the critical divide between physical dexterity and digital immersion, positioning the OOBI as a potential technology for next-generation metaverse ecosystems where human-machine interaction becomes as intuitive as natural touch.

2. Results and Discussion

2.1. Design and Working Principles of the Ambient EM Energy Powered Sensing Interface

EM radiation, as a ubiquitous and wasted energy in our daily life, has increasingly become a potential and convenient power source for portable devices.[30,31] Yet its potency in 3D perception and contactless interaction has not been explored. Here, a body-coupled ambient EM powered contactless sensing approach is investigated based on the OOBI (Figure 1a). Compared to air, which exhibits a significantly lower relative permittivity ($\varepsilon \approx 1$) and conductivity ($\sigma \approx 10^{-14}$ S m^{-1}), the human body demonstrates significantly high values for these properties ($\varepsilon \approx 78$ and $\sigma \approx 0.6$ S m^{-1}, respectively), rendering it an excellent medium for coupling EM energy.[32] As shown in Figure 1a, the dissipated EM signals are effectively captured by the human body and then transmitted to ground to form a close loop. When the human hands approach or touch the OOBI, the power of the EM signals will then partially go through the interface and then flow to ground through the measurement circuit, which forms another close loop.

To effectively capture the body-coupled EM signals, the OOBI is prepared with a transparent conductive layer and an insulation substrate. The conductive layer is polyvinyl chloride gel (PVC-gel), which is prepared by mixing PVC and dibutyl adipate (DBA) due to its excellent stretchability and proper resistivity. The insulation substrate is made of styrene ethylene butylene styrene (SEBS). Figure 1d exhibits the soft, thin, transparent, and stretchable characteristics of the interface. The transmittance of the PVC-gel with SEBS is shown in Figure S1 (Supporting Information), which achieves over 70% transmittance across both visible and infrared spectra. Meanwhile, the resistivity and the maximum elongation of the interface with different ratios of materials composition are shown in Figure 1e. The stress–strain curves of the PVC-gel with different PVC:DBA ratios is also presented in Figure S2 (Supporting Information). PVC gel with PVC:DBA ratios of 1:0.5, 1:1, 1:1.5, 1:2, 1:3, and 1:4 exhibits Young's moduli of 58, 10, 6.1, 1.5, 0.76, and 0.51 MPa, respectively. These results quantitatively confirm the progressive mechanical softening induced by increasing DBA concentration. However, with the increase of DBA, the elongation at break first increased and then decreased. This trend arises from DBA's dual role as both plasticizer and structural modifier. At moderate concentrations, DBA molecules intercalate between rigid PVC chains, expanding intermolecular distances and weakening chain interactions.[33] The resultant enhancement in chain mobility effectively plasticizes the matrix, increasing ductility. Therefore, the PVC-gel becomes softer with more DBA. However, excessive DBA introduction induces over small interaction forces, which will cause the gel more susceptible to breakage. FT-IR analysis of pure PVC, DBA, and PVC-gel composites confirmed the physical dispersion of DBA plasticizer within PVC polymer chains, with no spectroscopic evidence of specific intermolecular bonding (Figure S2, Supporting Information). To ensure both low modulus and high breaking elongation of the conductive layer, SEBS is adopted as the substrate, which effectively improves the stretchability of PVC-gel (Figure S3, Supporting Information). Moreover, due to the high mobility of the PVC chains, the resistivity of the composite is also improved. As shown in Figure 1e, the resistivity of the PVC-gel spans from 8.8 MΩ m (PVC:DBA = 1:0.5) to 39 kΩ m (PVC:DBA = 1:4). Regarding the sensor's stretchability and electro-mechanical stability, comprehensive characterization was performed, with key results presented in Figure S4 (Supporting Information). To evaluate the stretchability, we directly compared PVC gel with and without the SEBS substrate. The data reveal that the PVC gel without SEBS maintained functionality only up to 200% strain, beyond which fracture occurred at 300% strain, resulting in irreversible degradation of its mechanical and electrical properties. In contrast, the SEBS-incorporated sensor exhibited stable performance under 360% strain for ≈5000 cycles. This robust behavior conclusively validates the sensor's superior stretchability and electro-mechanical stability. Figure S5 (Supporting Information) demonstrates that the fabricated device maintains structural integrity at 433% strain.

The electrodes of the OOBI are placed on the four corners of the conductive layer as depicted in Figure 1f. This setting allows spatial perception of the OOBI, which will be elucidated in the following section. When the interface is touched, the four electrodes acquire body-coupled EM signals with varying amplitudes due to the resistance differences between the electrodes and the touch point (Figure 1f,g). For better understanding, the equivalent circuit model of the body-coupled EM signals transmission is shown in Figure 1h. The OOBI can be recognized as four parallel resistors according to Figure 1f. It is worth noting that the coupling between the human and the OOBI is bimodal, depending on whether the interface is touched (resistive coupling) or not (capacitive coupling). Consequently, the output of the OOBI can vary dramatically depending on the coupling modes.

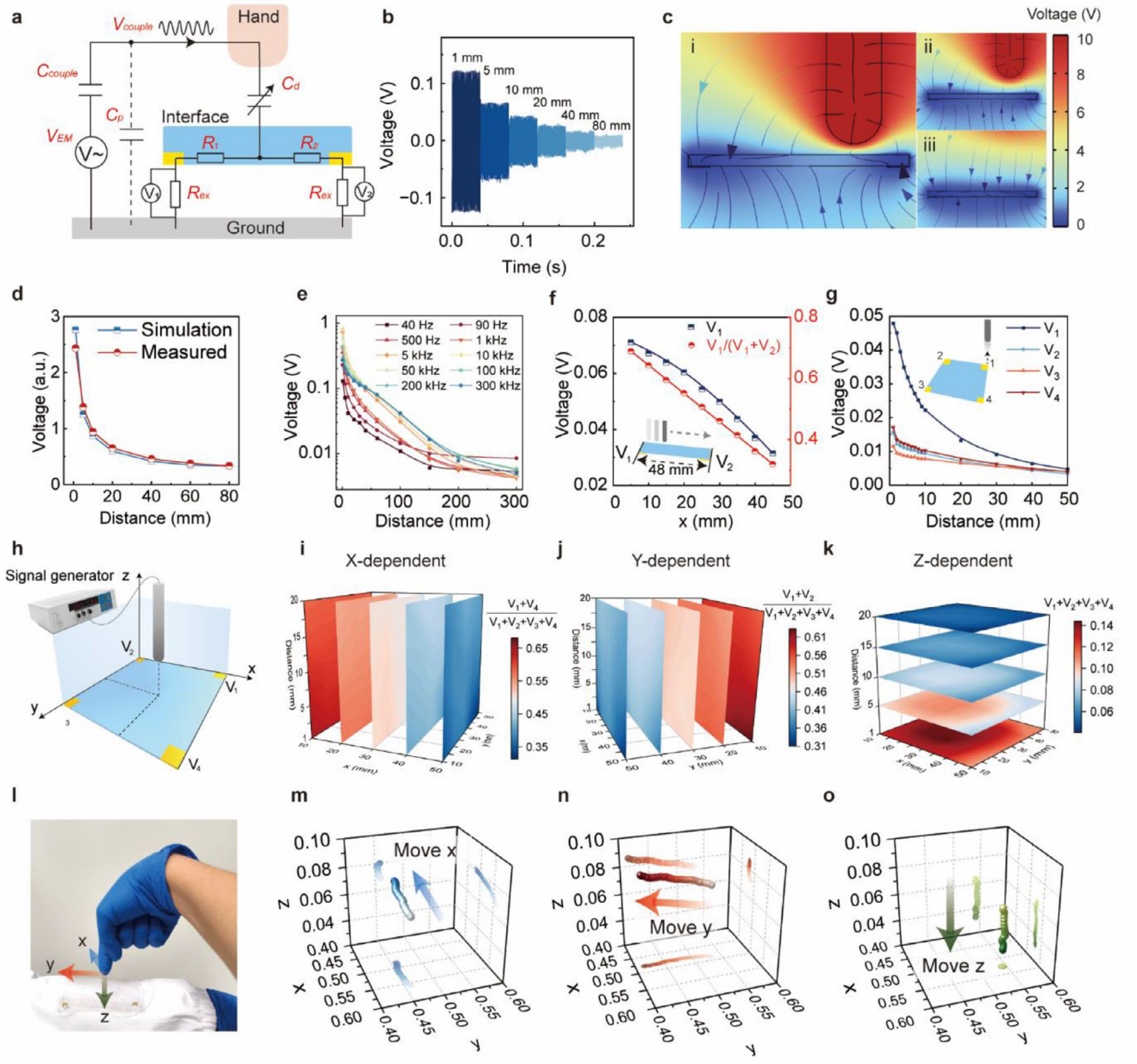

Figure 2. Spatial contactless sensing ability of the OOBI. a) Simplify the physical model of the contactless mode of the OOBI. b) Signal output of the OOBI at different distances between the EM source and the interface. c) Simulation of the influence of the distance between finger and interface on the electric field distribution. d) Signal amplitude comparison of the OOBI at different distances from the simulation and experiment results. e) Voltage response of the sensor at different distances with varied source frequencies. f) Variation of voltage amplitude and ratio from the OOBI when the EM source is placed on different positions at a 1 mm distance. g) Voltage amplitudes of four electrodes at different distances between finger and electrode 1. h) Illustration of experiment settings. i–k) Distribution of $(V_1+V_4)/(V_1+V_{2+}V_3+V_4)$ (i), $(V_1+V_2)/(V_1+V_{2+}V_3+V_4)$ (j), and $V_1+V_{2+}V_3+V_4$ (k) at different spatial positions. l A finger swipe through the OOBI. m–o) Reconstructed moving trajectory of the finger swiping through the OOBI at *x* (m), *y* (n), and *z* (o) direction.

2.2. Mechanisms of Spatial Contactless Sensing Ability of the OOBI

When the OOBI works on the capacitive coupling mode, it can achieve contactless sensing. The contactless sensing process of the OOBI is elucidated using a simplified physical model, and its corresponding equivalent circuit is illustrated in **Figure** 2a. The model can be divided into four parts: the human hand, the surface of interface, the electrodes of interface, and the ground. Here, V_{EM} is the voltage of ambient EM sources; C_{couple} represents the spatial coupling capacitance between human body and the EM source; V_{couple} denotes the body-coupled voltage output of the hand; C_p is the parasitic capacitance between the hand and the ground; C_d denotes the couple capacitance between the hand

and the interface; R_1 and R_2 are the resistances between two electrodes of interface and the surface of the interface closest to the hand; R_{ex} is the internal resistance of measurement circuit. According to this model, the distance $d(t)$ between the hand and the interface determines the value of C_d, which will directly influence the voltage outputs of the electrodes.

The voltage output of the OOBI under different distances between the hand and the interface is measured as shown in Figure 2b. To further investigate the mechanism of contactless sensing of the OOBI, COMSOL-based finite element method simulations are performed (Figure 2c). As shown in Figure 2c(i)–(iii), the position of hand strongly affects the distribution of the electric field, and thereby changes the voltages of the electrodes.

For ease of understanding, the OOBI with only a single electrode is considered (Figure S6, Supporting Information). According to Note S2 (Supporting Information), the voltage of the electrode can be described as:

$$|V_{out}| = |V_{couple}| \cdot \frac{R_{ex}}{\sqrt{\left(R_{ex}+R_i\right)^2 + \frac{d^2}{\left(\varepsilon\varepsilon_0 Sw\right)^2}}} \quad (1)$$

Therefore, the relationship between $d(t)$ and the voltage output exhibits an inverse exponential pattern, which is demonstrated on the simulation and experiment results (Figure 2d). The output of the OOBI can be influenced by the interface's resistance and the source's frequency. Thus, to further improve the performance of the OOBI, several experiments are executed to investigate the impacts of these parameters.

First of all, under a sinusoidal electric field with a peak value of 20 V, the relationships between distance and voltage output of the OOBI prepared with different PVC:DBA ratios are compared in Figure S7 (Supporting Information). It can be observed that the body-coupled voltage remains relatively high when the ratio of PVC to DBA is within the range of 1:1 to 1:3. Therefore, considering both flexibility and performance comprehensively, the ratio of PVC and DBA is set as 1:3 in the following experiment.

Figure 2e illustrates the relationship between distance and the detected voltage signal under various frequencies of the source signal. Here, the frequencies adopted 40 and 90 Hz to avoid the interference of 50 Hz ambient noise from other equipment. The results indicate that as the frequency increases, the attenuation imparted by distance to the source signal gradually diminishes. Consequently, the non-contact sensing distance of the OOBI also increases with rising frequency. This observation is corroborated by Equation (1), which suggests that as w increases, the influence imparted by d decreases, aligning with the experimental outcomes. However, this trend fades away when frequencies exceed 50 kHz. This saturation is attributed to the fact that the voltage induced by human body coupling is also influenced by frequency. As depicted in Figure 2a, the impedance arising from parasitic and coupling capacitors decreases with increasing frequency, which in turn reduces the voltage generated by human body coupling. Meanwhile, the result reveals that OOBI's electrical output and distance remain significantly correlated in the range of more than 200 mm when the source frequency exceeds 500 Hz. This verifies the wide proximity sensing range more than 200 mm of the OOBI.

Apart from the proximity sensing ability, the OOBI can detect the spatial position because of the multi-electrode design as shown in Figure 2a. The difference between R_1 and R_2, which are determined by the hand position, will influence the electrodes' voltage output. As illustrated in Figure 2f, the voltage output from electrode 1 decreases as the distance of the hand to the corresponding electrode increases. Meanwhile, the ratio $V_1/(V_1+V_2)$ exhibits superior linearity, which means that the ratio can be used as an excellent indicator of position. To achieve 3D spatial positioning, four electrodes design is applied the OOBI here. In Figure 2g, the variation of the voltage outputs of four electrodes under different distance of source is drawn. Apparently, there is a significant relationship between the outputs of the four electrodes and the spatial position of the source. To explore the rule behind the phenomenon, the voltage output under different spatial positions (5 × 5 × 5 points) is detected as depicted in Figure 2h. Inspired by the linearity of the ratio in Figure 2f, the distribution of the ratios of four voltages and their sum are plotted (Figure 2i–k). It is worth noting that the ratio of $(V_1+V_4)/(V_1+V_{2+}V_3+V_4)$ is highly correlated with x and insensitive to variations in y and z (Figure 2i). Similarly, the ratio of $(V_1+V_2)/(V_1+V_{2+}V_3+V_4)$ is highly correlated with y and insensitive to variations in x and z (Figure 2j). Besides, the sum of four voltages also exhibits the same characteristic (Figure 2k). These indicate that these three different ratios can act as the indicators of x, y, and z, respectively. To verify the performance of these indicators, we use them to real-time track the trajectory of a finger as illustrated in Figure 2l–o. The reconstructed trajectory demonstrates the effectiveness of the indicators and presents the potential of spatial positioning ability of the OOBI. Compared with the traditional sensing arrays that require a mass of electrodes, the OOBI only needs 4 electrodes to achieve precise 3D positioning, which significantly reduces the cost of system complexity. The comparison between the OOBI and the existing state of the art contactless perception e-skins is given in Table S1 (Supporting Information).

2.3. Mechanisms of Tactile Sensing Ability of the OOBI

Except for contactless sensing ability, the OOBI can also perceive precise tactile information, which is important for the precision control field. Unlike the contactless mode, a resistive coupling is formed between the finger and the interface when a human touches the interface (**Figure 3a**). Therefore, the coupling voltage from the human body can transmit to interface with much less attenuation, which is further visualized in the simulation result (Figure 3b). This feature can be used as a sign to distinguish tactile and contactless sensing, which has been a challenge in previous researches, due to the overlap of the output signals in both modes, including capacitive and magnetic driven non-contact sensor.[34]

The sum of voltage signal outputs of the four electrodes is presented in Figure 3c, according to which the difference between contact and non-contact is significant, demonstrating the practicability to use the voltage output to distinguish tactile and contactless sensing modes. Meanwhile, the voltage amplitude of the OOBI also exhibits its capability to detect the force. As shown in Figure 3d, we systematically characterized the force-voltage

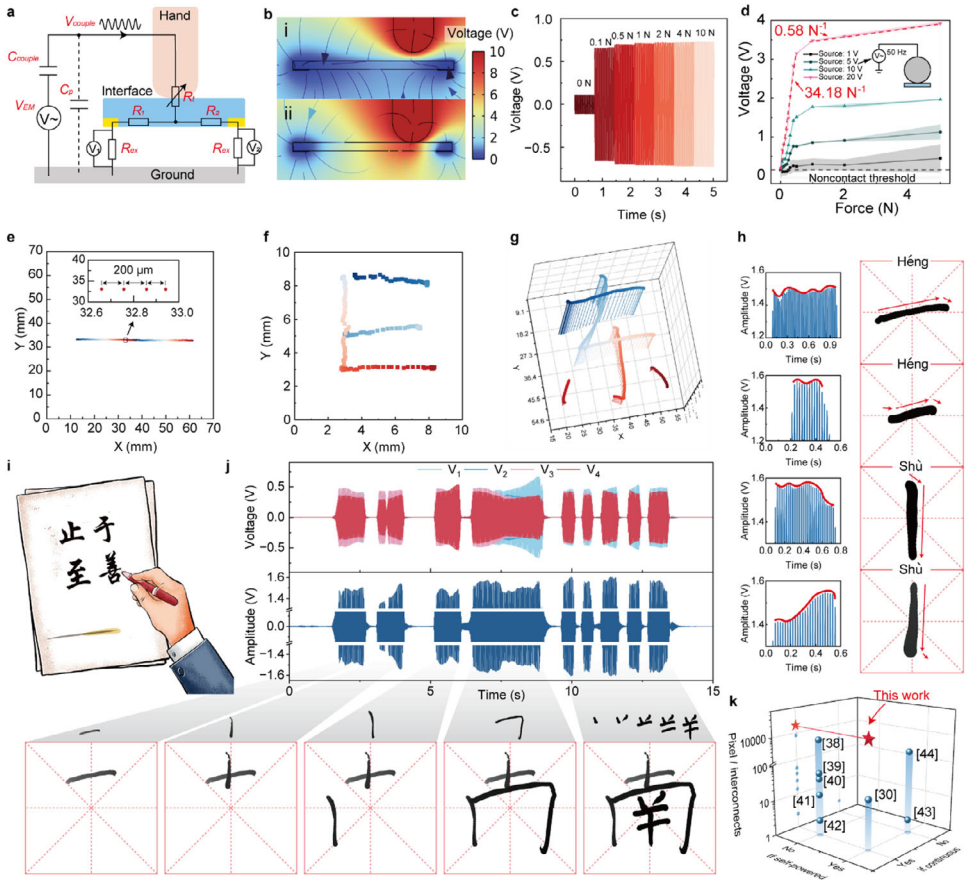

Figure 3. Calligraphy-grade high-resolution 2D tactile sensing capability. a) Simplify physical model of the tactile mode of the OOBI. b) Simulation of the influence of the touch of a finger on the interface. c) Sum of the voltage outputs of the four electrodes at different forces exerted on the interface, which shows the significant difference between contact and non-contact. d) Force-voltage relationship under sources (50 Hz sinusoidal signal) with different amplitudes (1, 5, 10, 20 V). e) Reconstructed positions of points with a gap of 200 μm using the isoline theory. f) Reconstructed letter "E" using the isoline theory. g) Reconstructed Chinese character "Dong" using the isoline theory. h) Reconstructed writing stroke of Chinese characters "Heng" and "Shu" with different variation of strength. i,j) Application of writing calligraphy-grade Chinese characters. k) Benchmark comparison highlighting the proposed e-skin ratio of pixel to electrodes, self-powered ability, and sensing continuity compared to existing e-skins.[30,38–44]

relationship of OOBI using a spherical sponge probe (elastic modulus ≈ human fingertip, diameter = 1.5 cm) with conductive aluminum electrodes. Measurements were conducted across multiple pressure cycles (five times), with error bands now indicating measurement variability. The characteristic response exhibits a steep voltage rise during initial contact (0–0.5 N) and then close to a saturation area. This behavior originates from contact mechanics: The soft sponge probes undergo rapid deformation at low pressures, maximizing sensitivity in the 0–0.5 N range. And the probes will meet a saturation of contact area at higher pressures, which explains the signal plateauing. According to Figure 3d, the output voltage of OOBI would vary under different sources. Therefore, it is not feasible to distinguish tactile and contactless sensing modes by setting a fixed threshold value. In practical usage, during intentional finger interactions, applied pressures consistently exceed 0.4 N (validated in Figure S8, Supporting Information for click/slide/light touch/press gestures). It is notable that the output signal amplitude surpasses non-contact levels by >400% when the load is more than 0.4 N (voltage of source ≥ 5 V). Therefore, in order to effectively distinguish between contact and non-contact and maintain sufficient redundancy, the threshold of switching can be set to 1/3 of the voltage value at the maximum force state (>4 N), which can ensure that the dual-mode switching can be effectively carried out in practical applications without switching problems.

Other than the spatial positioning and force detection ability of the OOBI, it is also able to precisely monitor the 2D trajectory. Existing approaches[30,35,36] that utilize four electrodes for positioning adopt voltage ratios as approximations for the abscissa x and the ordinate y. However, this method is an approximation of the positioning point, which incurs significant errors in regions close to the four electrodes, thereby resulting in notable character distortions. To achieve high-precision handwriting reconstruction and avoid character distortions arising from approximation estimates, we propose a four-electrode handwriting reconstruction algorithm based on the isoline method, which is proposed by Sun et al.[37]

First, we employed a customized three-axis control platform to make contacts at equally spaced locations across the interface and collected the voltage amplitudes corresponding to four

electrodes. As illustrated in Figure S9 (Supporting Information), we gathered voltage amplitudes for an 11 × 11 grid of equally spaced points. Subsequently, we calculated two ratios, R1 = $(V_1+V_2)/(V_1+V_{2+}V_3+V_4)$, and R2 = $(V_1+V_4)/(V_1+V_{2+}V_3+V_4)$, for these points (Figure S10, Supporting Information). The rationale behind selecting these two ratios as key parameters stems from their inherent relationship with the x and y coordinates of the contact points, which aligns with the reasons cited in previous studies that utilized these ratios.[30,35,36] In contrast to previous approaches that directly employed these ratios as coordinates, we computed the isoline distributions of these ratios across the entire interface, as depicted in Figure S11 (Supporting Information). This process yielded isoline distribution matrices for the interface. When a contact is made at an unknown point, the corresponding two ratios can be computed. By referencing these ratios in the previously obtained isoline matrices, we can locate the two isolines corresponding to these ratios and determine their intersection point, thereby obtaining the coordinates of the contact point (Figure S12, Supporting Information). The whole process is illustrated in Figure S13 (Supporting Information). This method effectively mitigates the distortion issues encountered in previous work and achieves a higher level of positioning accuracy. In Figure 3e, we used the three-axis control platform to touch the OOBI with a gap of 200 µm. Derived from the four-voltage output from the electrodes of the OOBI, the touch point can effectively reconstruct these touch points, which reveals that the OOBI can achieve a high resolution of less than 200 µm. To address the quantitative evaluation of trajectory accuracy, root mean square error (RMSE) between reconstructed and ground-truth positions was analyzed, with results presented in Figure S14 (Supporting Information).

Based on the high-resolution tactile sensing capability, the OOBI can be used as a high-precision writing interface. Here, the letter "E" and corresponding Chinese character "Dong" are writing based on the OOBI, as shown in Figure 3f,g. Meanwhile, on the basis of its force sensing ability, the OOBI is able to capture the strength variation during the writing process, which is crucial for Chinese calligraphy. Specifically, in Chinese calligraphy, strength has a great impact on the aesthetics of the overall text. As depicted in Figure 3h, for the writing stroke, "Heng" and "Shu", the reconstructed results can effectively present the variation of strength of writing strokes by the thickness. Meanwhile, the details of the trajectory are also well presented as denoted by the red arrows. In Figure 3i,j, the application of writing Chinese characters is demonstrated. To better highlight the unique benefits of trajectory tracking and force sensing, a video showcasing real-time Chinese handwriting is shown in Movie S1 (Supporting Information). This application vividly illustrates the precise capture of writing stroke and synchronized pressure-level detection. These results reveal the calligraphy-grade tactile sensing ability and its potential for high precision application. Critically, this bimodal sensing capability extends beyond artistic applications—it enables tamper-resistant electronic signatures by binding biometric pressure profiles to trajectory patterns, a feature unattainable with cameras or touchscreens. Figure 3k compares the ratio of pixel to electrodes, self-powered ability, and sensing continuity among the OOBI and other outstanding e-skins, demonstrating its superior spatiotemporal resolution with fewer electrodes, low power consumption, and great continuity.

2.4. OOBI Enabled Complex 3D Gesture Recognition

Traditional human-computer interaction methods, such as keyboards, mice, or touchscreens, although satisfying people's needs to a certain extent, appear to be insufficiently natural and intuitive in some scenarios. Especially in immersive environments like VR and AR, users prefer to interact with the virtual and real environment through natural gesture movements. Herein, leveraging the intelligent processing capabilities of AI and the spatial perception abilities of the wearable OOBI devices, we come up with a new solution for immersive 3D gesture recognition applications.

Figure 4a illustrates the wearable application setup for the OOBI. To realize the wearable application while avoiding direct interference from signals emanating from the bottom of the device, we have implemented a grounding protection design. In this setup, the wearable interface is placed on clothing, with a flexible aluminum electrode connected to the ground placed underneath the clothing. An additional layer of insulating clothing is placed beneath the aluminum electrode to create isolation from the human skin. Regarding circuit connections, the ground used for shielding interference is connected to the circuit ground. The four electrodes of the OOBI are connected to a multi-channel ADC acquisition circuit based on the ADC7606 chip. Subsequently, several characteristic parameters are calculated using a coordinate algorithm and then input into a CNN-based machine learning model.

We chose 12 common gestures along with the frequently used 26-letter air-writing gestures to demonstrate the accurate recognition capabilities of the OOBI across multiple gestures. Beyond these gestures, the system can be extended to recognize other gestures as well. Specifically, the signals of a subset of these gestures, when calculated as coordinates in the manner depicted in Figure 2i–k, yield results as shown in Figure 4b. By observing the coordinate variation curves of several gestures, it is evident that the patterns of these curves can effectively distinguish between different motion characteristics. Compared to curves, convolutional neural networks (CNNs) excel at extracting features from images, enabling accurate identification for multi-class classification problems. Figure 4c illustrates the process of transforming the output of coordinate variation curves into multiple images containing time and frequency features information, which are then fed into a neural network model with a residual network (ResNet) structure, thereby achieving the entire workflow from curve analysis to image-based gesture recognition. Specifically, when converting the input signal into an image, we utilize the continuous wavelet transform (CWT) to fully preserve the time-frequency characteristics of the signal. On the other hand, due to the insensitivity of the CWT to the positive-negative symmetry of time-frequency signals, which is crucial information for spatial gesture signals, we also convert the positive-negative information of the signal into an image, as depicted in Figure 4c. This image, combined with the output of the CWT, forms the composite image input, which is then fed into the network (some samples are displayed in Figure S15, Supporting Information).

For the training dataset, gesture data were collected from 3 distinct volunteers to incorporate biological variability. Meanwhile, every gesture was performed more than 20 times to ensure a large enough dataset. Participants performed each gesture at

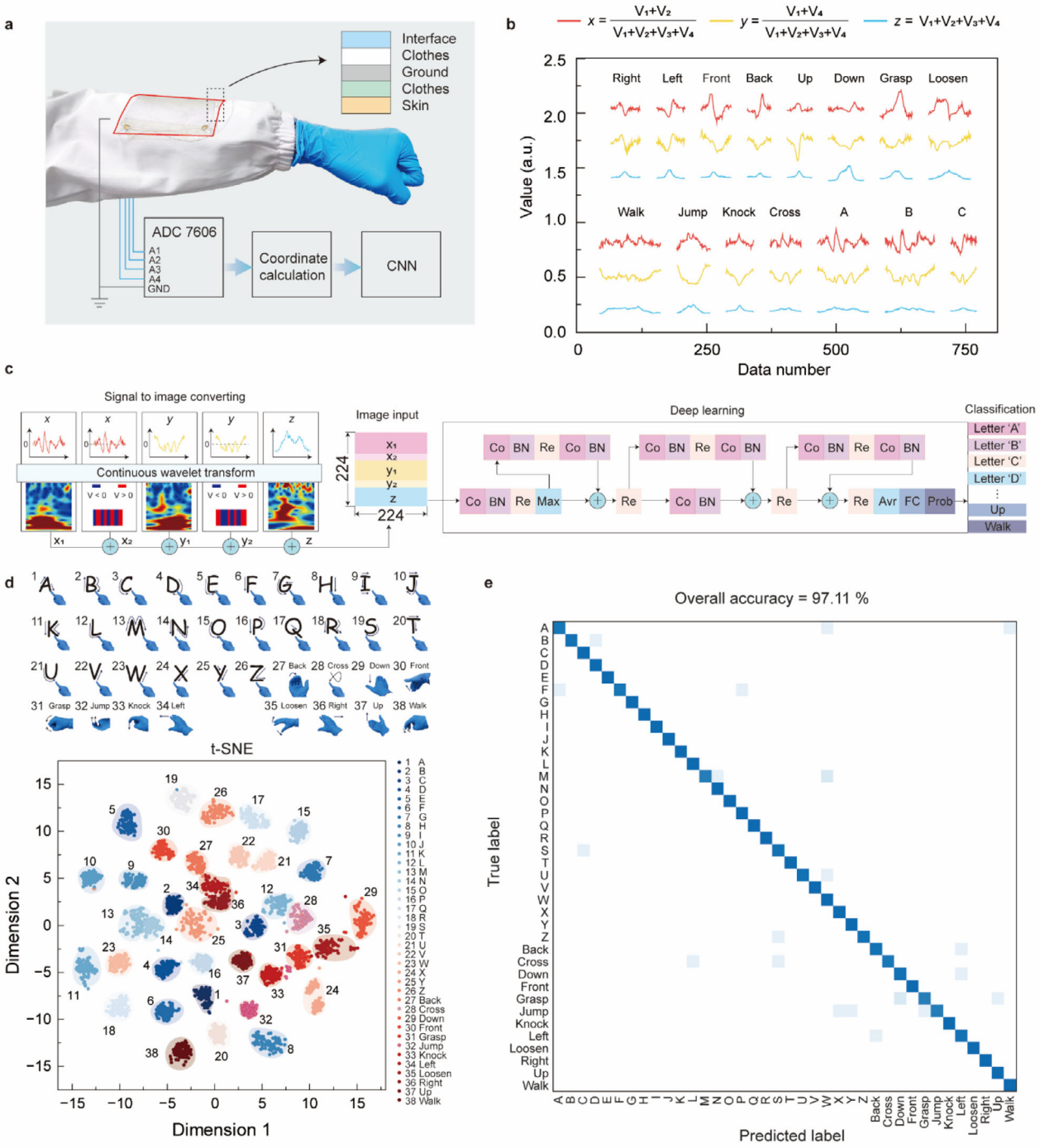

Figure 4. Non-contact spatial complex gesture recognition based on the OOBI. a) Wearable application setup for the OOBI. b) Samples of the calculated coordinate's variation from different spatial gestures. c) Workflow of transforming the signals into images and the structure of the proposed neural network, Co: Convolution layer, BN: Batchnorm layer, Re: ReLu layer, Max: Maxpool layer, Avr: Averagepool layer, FC: Fullconnect layer, Prob: Softmax layer. d) The t-SNE results of the trained network. e) A simplified confusion matrix with an average accuracy of 97.11%.

self-selected speeds to ensure the variability of gestures (no temporal constraints imposed). During the neural network training, the collected dataset is split with ≈80% for training and 20% for testing. We employ the t-distributed stochastic neighbor embedding (t-SNE) method to visualize the data derived from CNN outputs (Figure 4d). The result reveals the network's capability to distinguish between different action features. Figure 4e shows the proposed neural network's high recognition precision (97.11 %) among 38 different gestures.

Meanwhile, the reliability of the system in practical application is important.[45] To validate the wearable system's stability under dynamic conditions, we have implemented several experiments to characterize the output performance of the sensor under three states: normal state, bending state (bending radius: 4 cm), and stretching state (strain: 10%). According to the principle of bimodal interaction, the key parameters that decide the results are: R1 = $(V_1+V_2)/(V_1+V_2+V_3+V_4)$, R2 = $(V_1+V_4)/(V_1+V_2+V_3+V_4)$, and sum of voltage = $V_1+V_2+V_3+V_4$. As shown in Figure S16 (Supporting Information), the data reveal that bending and stretching alter parameter values, but relative trends among these parameters remain consistent. This may introduce positional offsets while preserving similar recognition patterns. Similarly, for non-contact gestures under these three states, key parameters R1, R2 , and sum of voltages exhibit comparable behavior. As shown in Figure S17 (Supporting Information), although curve shapes vary across states, their variation patterns maintain similarity, enabling effective gesture recognition when trend consistency is ensured. Regarding motion artifacts, contact-mode tests (Figure S18, Supporting Information) demonstrate that slight hand movements during wear increase fluctuations in these three parameters. While this introduces detection errors, such deviations remain tolerable under mild motion conditions.

2.5. Frequency-Dependent Object-Oriented Natural Human-Machine Interface

Traditional HMI methods, as illustrated in **Figure 5**a, employ distinct control interfaces tailored to different control objects. This approach increases the learning cost for users when operating various machines and diminishes the convenience of operation. In response to this issue, we propose an object-oriented natural HMI method that relies on EM wave frequencies.

In practical applications, EM interference generated by equipment exhibits distinct frequency signatures across device categories. For instance, wireless communication devices like Wi-Fi routers and Bluetooth transceivers operate at 2.4 GHz for data transmission, while RFID systems employ lower frequencies of 125 kHz or 13.56 MHz for inventory tracking and contactless transactions. Power cables generate 50/60 Hz electromagnetic fields from AC current flow, whereas electric motors produce high-frequency PWM noise spanning ≈10 kHz to 10 MHz during operation. Figure S19 (Supporting Information) displays the amplitude of acquired signals under different environments, equipment, and distances. The data indicate that environmental devices generate substantial signal amplitudes. When maintaining sufficiently close proximity, these can provide adequate signal energy for the interface. These measurable electromagnetic signatures, spanning distinct frequency bands, serve as unique identifiers for device classification and differentiation in electromagnetic spectrum analysis. However, these signal amplitudes also introduce interference, reducing recognition accuracy. To address this, as stated in Section 2.4, we implement grounded shielding on the interface and circuits for noise immunity. As demonstrated in Figure S19 (Supporting Information), electromagnetic signals with proper shielding (blue) are suppressed to levels far below unshielded conditions, making interference significantly smaller than detectable amplitudes. Simultaneously, during practical use, these electromagnetic signals can still propagate to the interface surface through body coupling, maintaining high amplitudes. Thus, the interface achieves high-precision bimodal sensing (Figure S20, Supporting Information).

Here, for convenient demonstration, apart from utilizing the 50/60 Hz electromagnetic wave signal emitted by a computer, we also employed a signal generator to produce two sine wave signals, each with a peak-to-peak voltage of 20 V but differing in frequency at 1 and 2 kHz, respectively. These signals were connected to two aluminum foil electrodes, each with an area of 3×3 cm^2, and placed in proximity to a robot dog and a robotic arm, serving as the electromagnetic wave sources corresponding to these devices, as illustrated in Figure 5b. Based on this foundation, leveraging the sensitivity of the OOBI to electromagnetic signals enables the perception of distance between the OOBI interface and various sources of frequency band signals. When a specific object is detected to be sufficiently close, it is selected for subsequent control operations. This method of selecting objects exhibits exceptional efficiency and intuitive characteristics.

To visually demonstrate the spatial distribution of electromagnetic waves with different frequencies, we utilized COMSOL to simulate this scenario, as illustrated in Figure S21 (Supporting Information) and the accompanying Table S2 (Supporting Information). Figure 5c and Figure S22 (Supporting Information) present the spatial distribution of signal's maximum amplitude from three sources with different frequencies. It is evident from the Figures that as the distance from the signal source increases, the corresponding signal amplitude decreases. In practical applications, object selection operations are only executed when the signal amplitude of a specific frequency exceeds a certain threshold to enhance control accuracy, as indicated by the lined areas in Figure 5c. Figure 5d–f displays the voltage signal outputs measured near different signal sources, each representing a distinct control object. Figures S23 (Supporting Information) show the corresponding short-time Fourier transform (STFT) results, revealing a significant increase in the amplitude of the corresponding frequency components in the signals as they approach different signal sources. For better interpretation, a movie is provided to visualize the entire frequency-based object selection process (Movie S2, Supporting Information). Based on this intuitive multi-object switching mechanism that simulates face-to-face human communication, we can achieve efficient human-multi-machine collaboration, realizing highly effective and natural human-machine interaction (HMI). Actually, the resolution of the EM signature can achieve less than 15 Hz, as demonstrated in Note S3 and Figure S24 (Supporting Information), which means that the number of objects that can be controlled is not limited by the frequency resolution.

Subsequently, we demonstrate seamless bimodal interaction through a coordinated object transfer task between a robot dog and a robotic arm. The experimental workflow involves: 1) precision placement of an object (sphere) from a robotic arm to a quadruped robot dog's end-effector, followed by 2) autonomous delivery of the object by the quadruped platform to a designated operator. As detailed in Section 2.3, the OOBI achieves dynamic mode switching through threshold-based signal amplitude detection, enabling contact-driven manipulation and non-contact spatial guidance. Critical to this functionality is the

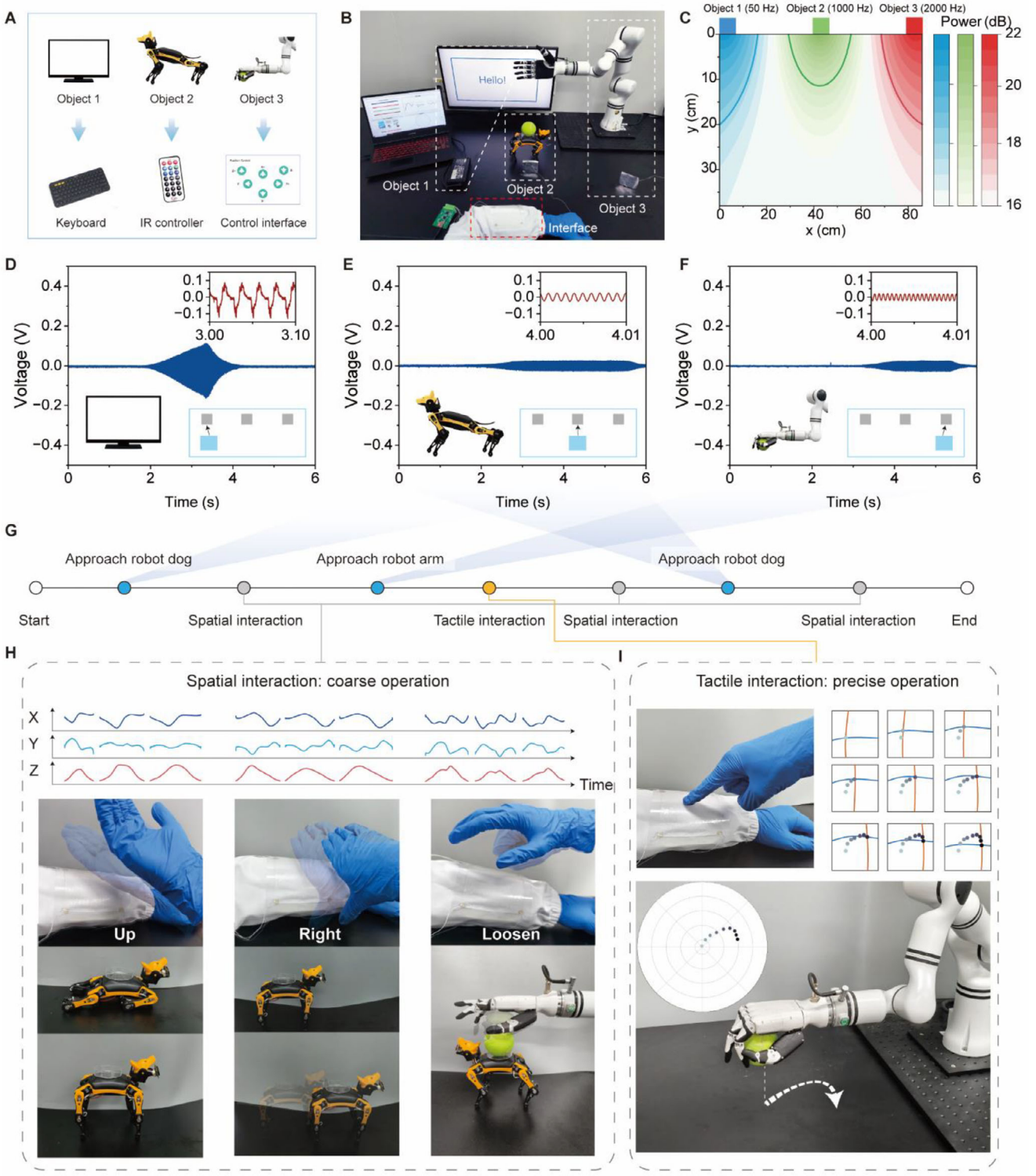

Figure 5. Frequency-dependent object-oriented natural HMI application. a) Traditional HMI methods using different control interfaces to control different objects, and each interface uses a complex button design to achieve multiple control instructions. b) Experiment settings for following frequency-dependent object-oriented natural HMI where the computer, robot dog, and robotic arm are respectively three different controlled objects. c) Simulation results reveal the spatial distribution of maximum amplitudes of the EM signals from three sources with different frequencies. d–f) Voltage signals output from the OOBI when approaching the (d) computer, (e) robot dog, and (f) robotic arm, where the insets show the signal details. g) Workflow of control multi-object using the OOBI. h) Spatial interaction using the OOBI for coarse operation. i) Tactile interaction using the OOBI for precise operation.

ultralow 0.6 ms response latency for mode transitions, and less than 10 ms response latency for sensor delay under 1 kHz electromagnetic excitation (Figures S25 and S26, Supporting Information), approaching the temporal requirements (<2 ms) for human-imperceptible interaction discontinuity. This ultrafast response speed satisfies the need for seamless switching of interaction modes. The CNN inference time is also counted as shown in Figure S27 (Supporting Information), which shows that CNN inference time remains below 20 ms.

As illustrated in Figure 5g and Figure S28 (Supporting Information), to control the robotic dog, the volunteer approaches the dog's signal source, enabling the OOBI to perceive the corresponding characteristic frequency signal and select the robot dog. Next, the 38 spatial manipulation gestures trained in the previous section are employed to control the dog's actions, such as standing up or turning right (Figure 5h). Subsequently, control is switched to the robotic arm by approaching it. To ensure the ball is accurately transferred from the robotic arm to the dog's back, the precise 2D tactile interaction method is used to control the robotic arm's spatial position, positioning the ball exactly where the dog is located and using spatial gestures to release the ball onto the dog's back (Figure 5i). Finally, the controlled object is switched back to the dog, instructing it to walk toward the volunteer. For easier understanding, the entire process is also demonstrated in Movie S3 (Supporting Information).

The above demonstration fully showcases the convenience brought by frequency-based object-oriented human-machine interaction in multi-object control scenarios. Compared to the traditional way shown in Figure 5a, which utilizes multiple distinct control interfaces and correspondingly complex and diverse commands, the OOBI proposed in this study allows for flexible coordinated control of multiple objects through a single, universal set of 2D tactile and 3D spatial perception gestures, significantly enhancing the interaction convenience and ease of manipulation in complex control scenarios. This innovates natural human-machine collaboration in complex environments and demonstrates the potential of object-oriented HMI in complex control contexts.

3. Conclusion

In this study, we present a transparent and stretchable HMI interface that successfully bridges the critical gap between high-precision manipulation and immersive interaction in metaverse systems. Based on body-coupled EM mechanism, we investigate the bimodal coupling (resistive coupling and capacitive coupling) between human and OOBI, and develop tactile sensing and spatial contactless sensing mechanisms. The OOBI's 2D tactile capability achieves dual-mode response for both force detection (34.18 N^{-1}) and trajectory reconstruction (200 µm spatial fidelity), enabling calligraphy-grade handwriting recognition. Remarkably, the system extends interaction dimensionality through a 200 mm operational range in non-contact mode, demonstrating exceptional 97.11% recognition accuracy across 38 gesture patterns encompassing the complete English alphabet. To address multi-object interaction challenges in complex environments, we develop an object-oriented HMI framework that enables single-interface control of multiple devices through EM signature recognition. This biologically inspired system mimics human social interaction patterns by automatically selecting proximate objects through their unique EM fingerprints, effectively eliminating manual switching between targets. The bimodal architecture further enhances operational efficiency by enabling seamless transitions (response time < 1 ms) between precision 2D manipulation and immersive 3D navigation based on real-time signal amplitude analysis. These innovations collectively establish a new paradigm for human-machine collaboration, effectively unifying physical dexterity with digital immersion. By achieving human-like intuitive interaction through natural gesture recognition and adaptive object selection, the OOBI framework reveals a potential blueprint for future natural intuitive interaction. Future developments will prioritize expanding the gesture lexicon alongside implementing AI-driven adaptive learning to enable personalized interaction experiences, while concurrently advancing hardware capabilities through electromagnetic direction-sensing interfaces that resolve signal azimuth/elevation angles via EM field characteristics—collectively establishing spatially aware "face-to-face" interaction paradigms where directional perception contextualizes gesture interpretation for human-like intuitive operation.

4. Experimental Section

Preparation of the OOBI: The OOBI was prepared with a transparent conductive layer and an insulation substrate. The conductive layer was a polyvinyl chloride gel (PVC-gel) prepared by mixing PVC and dibutyl adipate (DBA), due to its excellent stretchability and proper resistivity. The insulation substrate was made of styrene ethylene butylene styrene (SEBS).

Preparation of the OOBI—Preparations of the SEBS Substrate: The SEBS powder (Sigma–Aldrich, CAS: 66060-58-4) was mixed with n-Hexane (Aladdin, CAS: 110-54-3). The mixed solution was then stirred for 12 h to dissolve completely. The solution was then spin-coated on a glass substrate and dried at room temperature.

Preparation of the OOBI—Preparations of the Conductive Layer: The conductive layer was made of PVC and DBA mixed solution. The mixed solution was prepared by mixing commercial PVC powder (Scientific Polymer Products Inc., Mw 275 000, CAS: 9003-22-9), with DBA (Macklin, CAS: 105-99-7) as a plasticizer, and dimethylacetamide (DMF) (Macklin, CAS: 624-49-7) as the solvent. The weight fraction of PVC and DBA was decided according to the weight ratio required in the experiment, respectively. For example, a weight ratio of 1:3 means 6 and 18 wt.%, respectively. The obtained solution was then spin-coated onto the prepared SEBS substrate, and dried at 60 °C. After drying, the conductive layer with a SEBS substrate was then prepared.

Characterization: The voltage data was measured by an oscilloscope (Siglent SDS 6034 H10 Pro) with a 10 MΩ impedance. The force applied to the sensor and sensor's maximum elongation were quantified using a force gauge (Pubtester, TST-01H). The resistance was tested using a digital multimeter (Keithley, DMM 7510). The signal generator (Tektronix, AFG1022X) was adopted to generate sine signals with different frequencies (40–300 kHz). The position of probe during the spatial and tactile sensing experiments was controlled by a customized three-axis control platform. The multi-channel data collection was executed through a data acquisition board which was based on ADC 7606 chip, and the board would transmit the collected data to the computer through the serial port. The optical transmittance of the thin film was characterized using a Shimadzu UV-3600i Plus UV–vis–NIR spectrophotometer. The FT-IR analysis was performed by a Thermo Fisher Scientific Nicolet iS20 spectromter.

Robot Arm and Robot Dog Control: The robotic arm was purchased from Realman Intelligent Technology (RM65). A self-developed MATLAB program was designed to control the joint movement or posture movement of the robot arm, and then communicate with the robot arm through Ethernet. Meanwhile, the app can also receive and process the data from

a data acquisition board, which collects the multichannel voltage outputs of OOBI.

The robot dog was Bittle, which can be controlled through BLE module of MATLAB. A self-developed MATLAB program was written to send various commands to the robot dog and make it execute different actions.

Simulation: The finite element analysis (FEA) was conducted with commercial simulation software COMSOL. The details of the simulation could be found in Figure S11 and Table S2 (Supporting Information).

Supporting Information

Supporting Information is available from the Wiley Online Library or from the author.

Acknowledgements

J.H. and Y.X. contributed equally to this work. This work was supported by the National Key R&D Program of China (grant no. 2022YFB3603403, 2021YFB3600502); the National Natural Science Foundation of China (grant no. 62075040, 62301150, 623B2021); the Southeast University Interdisciplinary Research Program for Young Scholars (2024FGC1007); the Start-up Research Fund of Southeast University (grant no. RF1028623164); the Nanjing Science and Technology Innovation Project for Returned Overseas Talent (grant no. 4206002302) and the Fundamental Research Funds for the Central Universities (grant no. 2242024K40015).

Conflict of Interest

The authors declare no conflict of interest.

Data Availability Statement

The data that support the findings of this study are available from the corresponding author upon reasonable request.

Keywords

3D spatial sensing, body-coupled electromagnetic coupling, human-machine interaction, tactile sensing, trajectory reconstruction

Received: April 14, 2025
Revised: June 25, 2025
Published online:

[1] J. Qi, L. Yu, E. T. Khoo, K. W. Ng, Y. Gao, A. W. C. Kow, J. C. Yeo, C. T. Lim, *Nat. Electron.* **2024**, *7*, 1098.
[2] Z. Zhang, X. Guo, C. Lee, *Nat. Commun.* **2024**, *15*, 6465.
[3] T. Chen, Q. Shi, M. Zhu, T. He, L. Sun, L. Yang, C. Lee, *ACS Nano* **2018**, *12*, 11561.
[4] Z. Sun, M. Zhu, X. Shan, C. Lee, *Nat. Commun.* **2022**, *13*, 5224.
[5] T. Kamijo, A. J. J. M. van Breemen, X. Ma, S. Shanmugam, T. Bel, G. de Haas, B. Peeters, R. Petre, D. Tordera, R. Verbeek, H. B. Akkerman, L. M. Hagelsieb, F. de Roose, I. Lieberman, F. Yamaguchi, R. A. J. Janssen, E. A. Meulenkamp, A. J. Kronemeijer, G. H. Gelinck, *Nat. Electron.* **2023**, *6*, 451.
[6] Z. Liu, X. Hu, R. Bo, Y. Yang, X. Cheng, W. Pang, Q. Liu, Y. Wang, S. Wang, S. Xu, Z. Shen, Y. Zhang, *Science* **2024**, *384*, 987.
[7] D. Zhong, C. Wu, Y. Jiang, Y. Yuan, M.-g. Kim, Y. Nishio, C.-C. Shih, W. Wang, J.-C. Lai, X. Ji, T. Z. Gao, Y.-X. Wang, C. Xu, Y. Zheng, Z. Yu, H. Gong, N. Matsuhisa, C. Zhao, Y. Lei, D. Liu, S. Zhang, Y. Ochiai, S. Liu, S. Wei, J. B.-H. Tok, Z. Bao, *Nature* **2024**, *627*, 313.
[8] X. Guo, Z. Sun, Y. Zhu, C. Lee, *Adv. Mater.* **2024**, *36*, 2406778.
[9] Y. Yang, T. He, P. Ravindran, F. Wen, P. Krishnamurthy, L. Wang, Z. Zhang, P. P. Kumar, E. Chae, C. Lee, *Sci. Adv.* **2024**, *10*, adk7488.
[10] Y. Xu, Z. Sun, Z. Bai, H. Shen, R. Wen, F. Wang, G. Xu, C. Lee, *Nat. Commun.* **2024**, *15*, 6022.
[11] N. Bai, Y. Xue, S. Chen, L. Shi, J. Shi, Y. Zhang, X. Hou, Y. Cheng, K. Huang, W. Wang, J. Zhang, Y. Liu, C. F. Guo, *Nat. Commun.* **2023**, *14*, 7121.
[12] W. Wang, Y. Jiang, D. Zhong, Z. Zhang, S. Choudhury, J.-C. Lai, H. Gong, S. Niu, X. Yan, Y. Zheng, C.-C. Shih, R. Ning, Q. Lin, D. Li, Y.-H. Kim, J. Kim, Y.-X. Wang, C. Zhao, C. Xu, X. Ji, Y. Nishio, H. Lyu, J. B.-H. Tok, Z. Bao, *Science* **2023**, *380*, 735.
[13] J. Wang, X. Wei, J. Shi, N. Bai, X. Wan, B. Li, Y. Chen, Z. Jiang, C. F. Guo, *Nat. Commun.* **2024**, *15*, 7094.
[14] Y. H. Jung, T. X. Pham, D. Issa, H. S. Wang, J. H. Lee, M. Chung, B.-Y. Lee, G. Kim, C. D. Yoo, K. J. Lee, *Nano Energy* **2022**, *101*, 107610.
[15] L. Su, S. Kuang, Y. Zhao, J. Li, G. Zhao, Z. L. Wang, Y. Zi, *Sci. Adv.* **2024**, *10*, adq8989.
[16] C. Xu, Y. Song, J. R. Sempionatto, S. A. Solomon, Y. Yu, H. Y. Y. Nyein, R. Y. Tay, J. Li, W. Heng, J. Min, A. Lao, T. K. Hsiai, J. A. Sumner, W. Gao, *Nat. Electron.* **2024**, *7*, 168.
[17] H. Li, P. Tan, Y. Rao, S. Bhattacharya, Z. Wang, S. Kim, S. Gangopadhyay, H. Shi, M. Jankovic, H. Huh, Z. Li, P. Maharjan, J. Wells, H. Jeong, Y. Jia, N. Lu, *Chem. Rev.* **2024**, *124*, 3220.
[18] L. Chen, S. Karilanova, S. Chaki, C. Wen, L. Wang, B. Winblad, S.-L. Zhang, A. Özçelikkale, Z.-B. Zhang, *Science* **2024**, *384*, 660.
[19] J. Hong, Z. Rao, S. Duan, S. Xiang, X. Wei, Y. Xiao, Y. Chen, H. Sheng, J. Xia, W. Lei, C. Yu, Q. Shi, J. Wu, *Nano Energy* **2024**, *131*, 110327.
[20] J. Li, H. Wang, Y. Luo, Z. Zhou, H. Zhang, H. Chen, K. Tao, C. Liu, L. Zeng, F. Huo, J. Wu, *Nano-Micro Lett.* **2024**, *16*, 256.
[21] Z. Hui, Z. Zhang, Y. Wang, R. Zhang, X. Liu, M. Jiang, F. Ju, W. Hou, Z. Xia, D. Wang, P. Wang, Y. Pei, R. Yan, Y. Zhang, Q. Chen, W. Huang, G. Sun, *Adv. Mater.* **2024**, *36*, 2314163.
[22] J. Park, Y. Lee, S. Cho, A. Choe, J. Yeom, Y. G. Ro, J. Kim, D.-h. Kang, S. Lee, H. Ko, *Chem. Rev.* **2024**, *124*, 1464.
[23] W. Liu, Y. Duo, J. Liu, F. Yuan, L. Li, L. Li, G. Wang, B. Chen, S. Wang, H. Yang, Y. Liu, Y. Mo, Y. Wang, B. Fang, F. Sun, X. Ding, C. Zhang, L. Wen, *Nat. Commun.* **2022**, *13*, 5030.
[24] Q. Liang, D. Zhang, T. He, Z. Zhang, H. Wang, S. Chen, C. Lee, *ACS Nano* **2024**, *18*, 600.
[25] J. Zhou, *Nat. Commun.* **2024**, *15*, 9875.
[26] H. Zhou, W. Huang, Z. Xiao, S. Zhang, W. Li, J. Hu, T. Feng, J. Wu, P. Zhu, Y. Mao, *Adv. Funct. Mater.* **2022**, *32*, 2208271.
[27] Y. Du, P. Shen, H. Liu, Y. Zhang, L. Jia, X. Pu, F. Yang, T. Ren, D. Chu, Z. Wang, D. Wei, *Sci. Adv.* **2024**, *10*, adp8681.
[28] W. Cheng, X. Wang, Z. Xiong, J. Liu, Z. Liu, Y. Jin, H. Yao, T.-S. Wong, J. S. Ho, B. C. K. Tee, *Nat. Mater.* **2023**, *22*, 1352.
[29] Y. Pang, X. Zhu, T. He, S. Liu, Z. Zhang, Q. Lv, P. Yi, C. Lee, *Adv. Mater.* **2024**, *36*, 2404763.
[30] Y. Xia, Y. Zhu, X. Zhi, W. Guo, B. Yang, S. Zhang, M. Li, X. Wang, C. Pan, *Adv. Mater.* **2024**, *36*, 2308424.
[31] W. Yang, S. Lin, W. Gong, R. Lin, C. Jiang, X. Yang, Y. Hu, J. Wang, X. Xiao, K. Li, Y. Li, Q. Zhang, J. S. Ho, Y. Liu, C. Hou, H. Wang, *Science* **2024**, *384*, 74.
[32] J. Li, Y. Dong, J. H. Park, J. Yoo, *Nat. Electron.* **2021**, *4*, 530.
[33] H. Park, S. J. Oh, D. Kim, M. Kim, C. Lee, H. Joo, I. Woo, J. W. Bae, J. H. Lee, *Adv. Sci.* **2022**, *9*, 2201070.
[34] J. Ge, X. Wang, M. Drack, O. Volkov, M. Liang, G. S. Cañón Bermúdez, R. Illing, C. Wang, S. Zhou, J. Fassbender, M. Kaltenbrunner, D. Makarov, *Nat. Commun.* **2019**, *10*, 4405.
[35] C.-C. Kim, H.-H. Lee, K. H. Oh, J.-Y. Sun, *Science* **2016**, *353*, 682.
[36] R. Xu, M. She, J. Liu, S. Zhao, J. Zhao, X. Zhang, L. Qu, M. Tian, *ACS Nano* **2023**, *17*, 8293.
[37] H. Sun, G. Martius, *Sci. Rob.* **2022**, *7*, abm0608.

[38] Y. Cho, T. Kim, G. Kim, H. W. Do, S.-R. Kim, J.-W. Park, J.-M. Myoung, W. Shim, *Adv. Mater.* **2023**, *35*, 2305697.
[39] K. Kim, J.-H. Hong, K. Bae, K. Lee, D. J. Lee, J. Park, H. Zhang, M. Sang, J. E. Ju, Y. U. Cho, K. Kang, W. Park, S. Jung, J. W. Lee, B. Xu, J. Kim, K. J. Yu, *Sci. Adv.* **2024**, *10*, adr1099.
[40] K. Park, H. Yuk, M. Yang, J. Cho, H. Lee, J. Kim, *Sci. Rob.* **2022**, *7*, abm7187.
[41] J. Shi, Y. Dai, Y. Cheng, S. Xie, G. Li, Y. Liu, J. Wang, R. Zhang, N. Bai, M. Cai, Y. Zhang, Y. Zhan, Z. Zhang, C. Yu, C. F. Guo, *Sci. Adv.* **2023**, *9*, adf8831.
[42] Y.-C. Huang, Y. Liu, C. Ma, H.-C. Cheng, Q. He, H. Wu, C. Wang, C.-Y. Lin, Y. Huang, X. Duan, *Nat. Electron.* **2020**, *3*, 59.
[43] Y. Lee, S. Lim, W. J. Song, S. Lee, S. J. Yoon, J.-M. Park, M.-G. Lee, Y.-L. Park, J.-Y. Sun, *Adv. Mater.* **2022**, *34*, 2108586.
[44] M. Shi, J. Zhang, H. Chen, M. Han, S. A. Shankaregowda, Z. Su, B. Meng, X. Cheng, H. Zhang, *ACS Nano* **2016**, *10*, 4083.
[45] M. Xia, J. Liu, B. J. Kim, Y. Gao, Y. Zhou, Y. Zhang, D. Cao, S. Zhao, Y. Li, J.-H. Ahn, *Adv. Sci.* **2024**, *11*, 2304871.